Journal of Materials Processing Technology 241 (2017) 54–63

Contents lists available at ScienceDirect

Journal of Materials Processing Technology

journal homepage: www.elsevier.com/locate/jmatprotec

Applying electron backscattering diffraction to macroscopic residual stress characterisation in a dissimilar weld

K. Abburi Venkata [a,*], C.E. Truman [a], H.E. Coules [a], A.D. Warren [b]

[a] University of Bristol, Solid Mechanics Research Group, Department of Mechanical Engineering, Bristol BS81TR, UK
[b] University of Bristol, Interface Analysis Center, HH Wills Physics Laboratory, Bristol BS81TL, UK

ARTICLE INFO

Article history:
Received 16 September 2016
Received in revised form 3 November 2016
Accepted 4 November 2016
Available online 6 November 2016

Keywords:
EBSD
Dissimilar weld
Phase volume fractions
Phase dependent residual stresses
Neutron diffraction

ABSTRACT

Dissimilar metal welds are complicated in nature because of the complex microstructure characteristics in the weld fusion zone. It is often necessary to know the phase distribution in a dissimilar metal weld especially at the interface such as fusion zone and heat affected zone to be able to predict the behaviour of the joint and its fitness for service. In this paper, a dissimilar metal weld made between ferritic/martensitic modified 9Cr-1Mo steel (P91) and austenitic AISI 316LN stainless steel using autogenous electron beam (EB) welding was analysed. The weld fusion zone has a local segregation of bcc and fcc phases. The EBSD technique was applied to determine the volume fractions of each of these phases in the weld fusion zone. This information was incorporated into the analysis of neutron diffraction data from the weld zone, and the macro-scale residual stresses were calculated from phase-specific stresses arising from the welding process. The results indicate that the overall macroscopic residual stress distribution in the weld centre is predominantly compressive in nature driven by the solid-state phase transformation of the weld pool during rapid cooling, with tensile peaks pushed adjacent to the heat affected zone (HAZ)/Parent boundaries on both sides of the fusion zone.

1. Introduction

Dissimilar metal welds are often used in industrial applications and usually create a complex fusion zone that is essentially different from the parent materials. Dawson (2012) in his research has studied the interfaces in transition joints made between ferritic steels of different Cr percentages. Significant microstructural changes were reported between the base metals and the weld interface in his work. Mvola et al. (2014) have examined dissimilar joints in various steel families including case studies and concluded that the microstructure at the interface and HAZ has a major influence on the mechanical properties and performance of joint in service. Sun and Karppi (1996) have outlined the advantages of EB welding as a potential joining mechanism for dissimilar metals. However the need for extensive joint characterisation in terms of microstructure and suitability to service has been stressed. Barnhouse and Lippold (1998) researched the effects of weld microstructure on toughness and corrosion resistance in dissimilar welds between stainless steels and carbon steels. Shahid et al. (2015) observed through their studies on dissimilar friction stir welds that the microstructure of the weld can affect the tensile strength of the component due to the formation of intermetallic compounds which aid in crack initiation and propagation. Chatterjee et al. (2016) summarised through their findings that the physical and chemical dissimilarities between parent materials influence the formation of microstructure in a dissimilar metal weld. Ueji et al. (2013) based on their research on dissimilar welds concluded that the interface of the joint contained a multi-phased microstructure different from base materials. According to a case study conducted by Hajri et al. (2015) on dissimilar metal weld joint in a superheater tube, indicated that failure occurred on alloy steel side rather than stainless steel side because of decrease in creep strength and increase in hardness at the weld interface on alloy steel side as a result of the microstructure. Bala Srinivasan et al. (2006) described that the welded joint of a dissimilar metal weld between a duplex stainless and low alloy steel was significantly inferior compared to both base materials in corrosion resistance.

Another crucial and unavoidable consequence of welding process is the development of residual stresses in the welded structure arising from the differential expansion and contraction of the weld pool. This effect is even more pronounced in dissimilar metal welds, because of the significant differences in the thermo-physical and mechanical properties of the parent materials. As these residual stresses exert a strong influence on the mechanical response of

* Corresponding author.
E-mail address: k.abburivenkata@bristol.ac.uk (K. Abburi Venkata).

http://dx.doi.org/10.1016/j.jmatprotec.2016.11.003

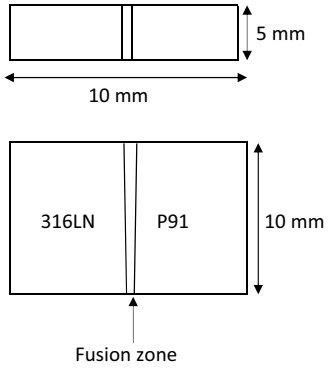

Fig. 1. Schematic representation of EBSD sample.

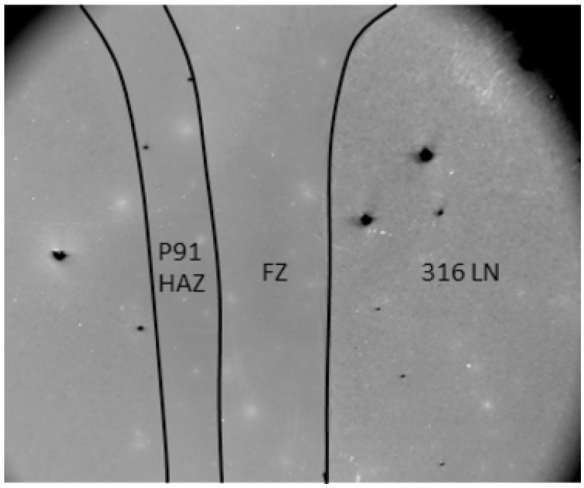

Fig. 2. Fusion boundary after mechanical polishing.

the welded joint during service, it is essential to quantify them. However the quantification is usually focussed on the macroscopic stresses alone. According to Stone et al. (2001), the usual approaches to calculating residual stresses in neutron diffraction involve either using a reflection plane that does not accumulate microstresses or use linearly combined lattice stresses such that the final reflection does not accumulate microstresses. However, in order to quantify the residual macrostress state arising from the welding process, it is crucial to identify the microstructure at the interface i.e., weld fusion zone and HAZ in terms of phase fractions and grain size.

Apart from being essential to the quantification of the macroscopic residual stress state via diffraction-based methods, the microstructure in the weld fusion zone and HAZ plays a critical role in failure. Especially in modified 9Cr steels, the microstructure at the interface has a significant influence on the creep performance of the joint and its susceptibility to Type IV failure. Abson and Rothwell (2013) based on their review on 9–12% Cr steels agreed that the fine grains in HAZ promote failure through void nucleation and/or cracking. Benjamin et al., 2009 carried out detailed microstructure evolution studies in P91 steel during fatigue and creep-fatigue conditions using EBSD. Based on the previous work done on dissimilar welds, it can be established that the joint characteristics in terms of microstructure are ordinarily extremely different from those of the parent materials and therefore need thorough characterisation to understand how these complex joints perform under the applied loads and what failure mechanisms they exhibit.

During the last decade many researchers have examined the residual stresses in welds using experimental and numerical approaches in dissimilar metal welds. Ferro and Berto (2016) attempted to quantify the residual stress state and crack-tip singularity at the weld root, in welded AA-6063 Al alloy, by determining the residual notch stress intensity factors (R-NSIFs) and local strain energy values due to thermo-mechanical loading. This method is an extension to the notch stress intensity factor (NSIF) evaluation method proposed by Lazzarin and Tovo (1998) for stress analysis in welds. Ohms and Martins (2014) investigated residual stresses in a thin slice extracted from a full-scale dissimilar metal piping mock-up using high energy synchrotron and neutron radiation. Ruiz-Hervias et al. (2014) examined residual stresses in ferritic to austenitic steel dissimilar laser weld using neutron and synchrotron radiation and identified that controlling the microstructure of the weld bead can mitigate the residual stresses introduced. Kerr et al. (2013) characterised residual stresses in a dissimilar metal weld nuclear reactor piping system mock-up using neutron diffraction, contour method, hole drilling and finite element predictions as a standardising procedure for determining weld residual stresses. However Lodini (2003) observed that when using diffraction based techniques, in a multiphase material such as the fusion zone of a dissimilar weld, the second order stresses averaged over one single phase are not usually equilibrated. Nevertheless, these stresses when summed over both phases in a bulk material should equal to zero, thereby making the macroscopic stress state as simply the combined macrostresses characteristic of each phase. This can be achieved if the corresponding volume fractions of the representative phases in the weld fusion zone are known.

EBSD is a microstructure investigation technique in the scanning electron microscope (SEM) that is rapidly becoming an extremely useful tool for the analysis of complex microstructures such as weld joints to identify the phases and gather information on the grain size and texture at the interface as stated by Randle (2009) in his

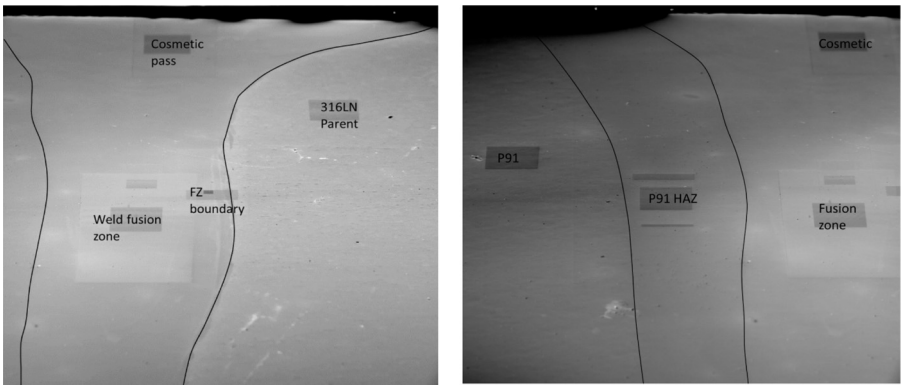

Fig. 3. Sampling area across the weld (a) 316LN HAZ/Parent (b) P91 HAZ/Parent.

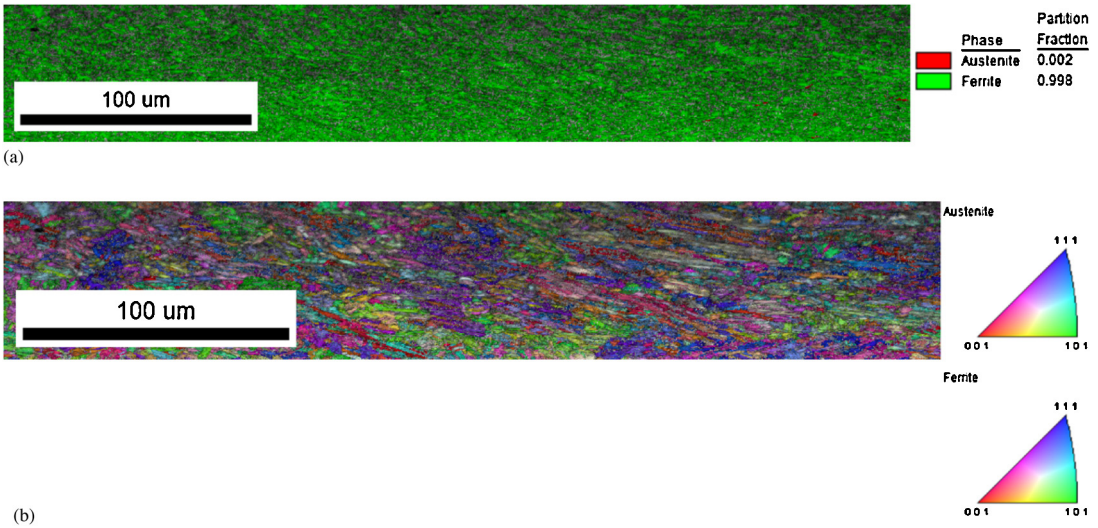

Fig. 4. (a) Phase map and (b) Orientation map for the weld fusion zone away from the cosmetic pass.

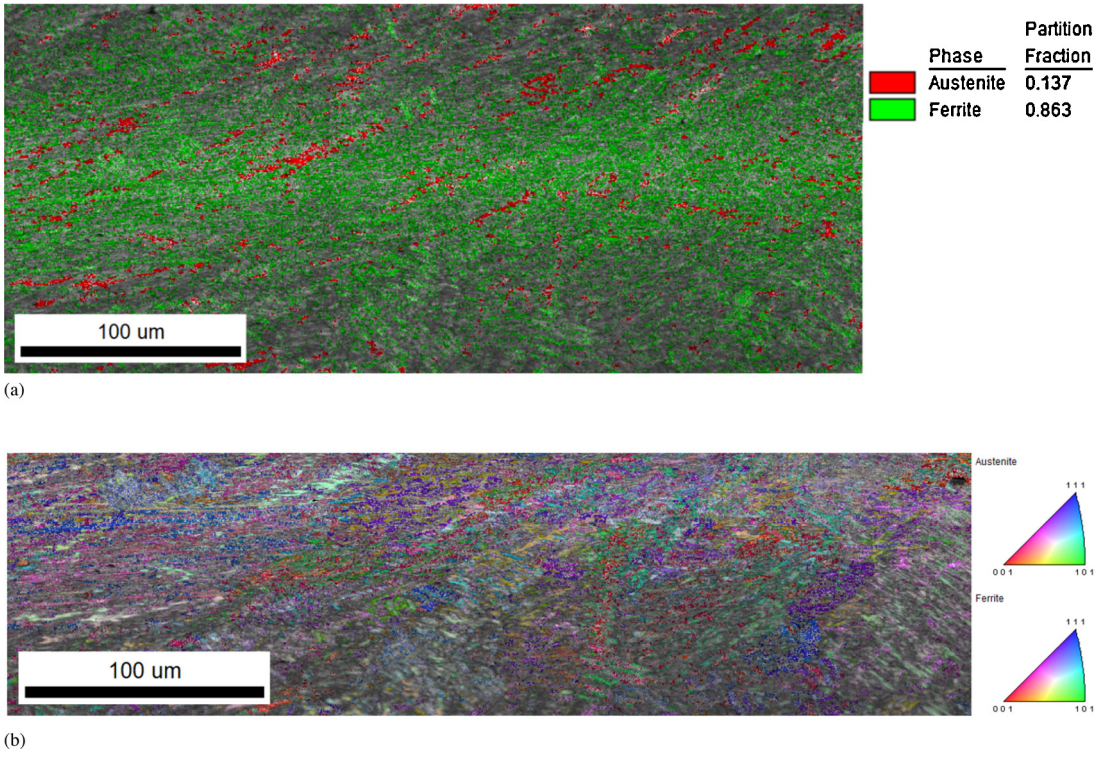

Fig. 5. (a) Phase map and (b) Orientation map for the weld fusion zone under the influence of cosmetic pass.

review. It has evolved into a comprehensive tool with a wide range of applications in texture mapping, grain boundary characterisation, local phase and lattice strain determination. Winkelmann et al. (2016) showed that EBSD is an important tool for analyzing crystallographic phases in materials. In the present paper, EBSD technique has been applied to a dissimilar weld joint between P91 ferritic steel and 316LN stainless steel using EB welding, to analyse the microstructure in terms of grain size and phase distribution in the fusion zone and HAZ. This information was then used to determine the macroscopic residual stress state in the fusion zone, from the phase dependent macrostresses measured by neutron diffraction on the welded plate, based on the identified phases and phase fractions. This paper attempts a holistic approach of microstructure-driven residual stress analysis to determine the macroscopic stress state in a dissimilar welded specimen. The details of the experiment and the final results are presented and discussed.

2. Sample

The specimen was extracted from a dissimilar metal weld made from P91 ferritic/martensitic steel and 316LN stainless steel using an autogenous electron beam welding. The details of the welding procedure were discussed in depth by Abburi Venkata et al. (2016) in their research on characterising this dissimilar joint through residual stress measurement using neutron diffraction and FE simulation. These details are only briefly explained here. The weld dimensions were 250 mm × 156 mm, with a nominal thickness of

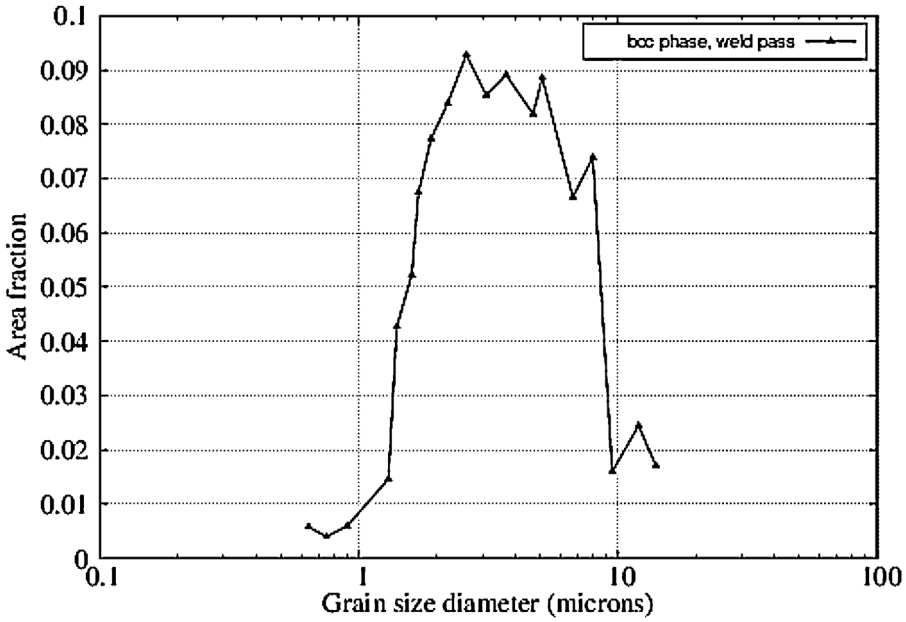

Fig. 6. Grain size plot for ferrite in the weld fusion zone without cosmetic pass.

Table 1
Chemical composition of the base metals in% wt. (Balance Fe).

Steel	C	Mn	Zr	Si	P	S	Cr	Mo	Ni	Cu	Al	N	Nb	Ti	V
P91	0.11	0.39	0.005	0.27	0.017	<0.003	8.82	0.82	0.21	0.17	0.02	0.0464	0.07	0.004	0.2
316LN	0.03	1.72	–	0.39	0.025	<0.003	17.5	2.58	11.9	0.195	0.001	0.087	0.005	0.005	0.051

11 mm. The weld was performed using two passes: one welding pass to join the plates followed by a 'cosmetic' pass using a defocussed beam to improve the surface profile and appearance of the weld bead. The weld pass had a full-depth penetration and the cosmetic pass had a 4.5 mm depth of penetration. The weld fusion zone and HAZ were ~1.1 mm and ~0.5 mm wide respectively. The specimen used for EBSD analysis was 10 mm x 5 mm x 10 mm in dimension and is extracted from the weld centre such that it has regions from the fusion zone, HAZ and the base metal on either side of the fusion zone. The schematic of the specimen is indicated in Fig. 1. The chemical composition of the base metals is provided in Table 1. The specimen was machined from the weld pad using high cooling rate to avoid any alteration of the microstructure from the machining process. The machined surfaces were then ground to ensure that the surfaces are flat.

3. Experimental setup

The experiment was conducted using a Zeiss Sigma HD VP Field Emission SEM at the Interface Analysis Centre (IAC), School of Physics in University of Bristol. The sample was prepared using consecutive silicon carbide grinding and diamond paste polishing. Further polishing using 0.1 μm colloidal silica was used approximately for 24 h to obtain a surface which was suitable for EBSD. The EBSD scans were performed by operating the SEM at 30 kV, in high current mode, with the specimen tilted by 70° to the horizontal. Orientation image mapping (OIM) data collection software (Ametek, Utah, USA) was used for the collection, processing and analysis of the EBSD data. Any stray pixels during data processing were removed using the **"cleanup"** function in the OIM software. Additionally, any points with a confidence index of less than 10% were removed from data analysis in order to avoid mischaracterisation of points and ensure a robust statistical analysis. In addition, in the OIM data analysis software, grain identification is based on clusters of pixels with a similar crystal structure and orientation. The software has an adjustable grain boundary misorientation limit which is used to define the edges of grains, for the data presented a boundary misorientation of 5° has been used (i.e. where two neighbouring pixels have a difference in orientation of 5° or more, the software interprets that as a grain boundary). Subsequent grain size calculations revolve around calculating the dimensions of the grains – the diameter is the mean diameter of all the grains of the relevant phase in the material.

The fusion boundary on the specimen after sample preparation is shown in Fig. 2. The sample was measured at various locations in the fusion zone and HAZ on the P91 side such that the reflections were obtained from areas corresponding to the weld fusion zone at mid-thickness (away from the cosmetic pass), weld fusion zone under cosmetic pass at a depth of 2 mm from top surface, P91 HAZ, P91 parent, 316LN HAZ and 316LN parent as shown in Fig. 3. The surface area measured is approximately 0.25 mm x 0.5 mm.

4. Results

Based on the diffraction pattern, the microstructure in the weld fusion and cosmetic pass regions as well as the HAZ/Parent on either side of the weld fusion zone were analysed and the percentage of ferrite and austenite as well as the grain size for each of these phases in the measured areas were determined. The inverse pole figure and phase maps obtained from the measured areas were used to study the microstructure and identify the volume fraction of the microstructural constituents austenite, ferrite and martensite.

The phase map and the orientation map from the weld centre well below the cosmetic pass are shown in Fig. 4(a) and (b) respec-

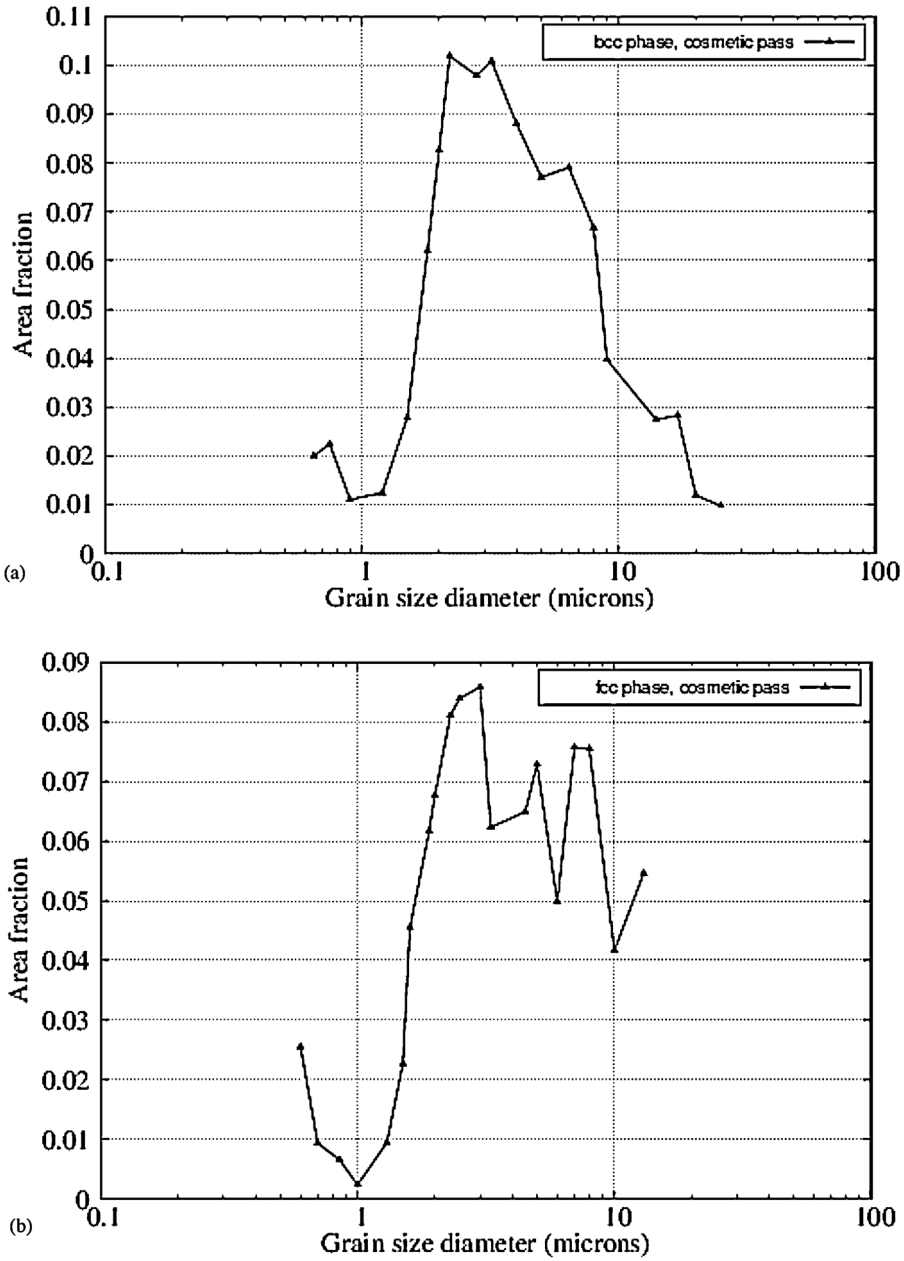

Fig. 7. (a) Grain size plot for (a) ferrite (b) austenite in the weld fusion zone with cosmetic pass.

tively and those for the region under the cosmetic influence are shown in Fig. 5(a) and (b) respectively. From Fig. 4(a), it can be observed that the weld fusion zone predominantly contains ferrite and traces of austenite. However observing Fig. 5(a), it can be seen that the percentage of austenite has been increased with an additional pass. Analysing the phase map, from Fig. 4(b), the volume fractions of ferrite and austenite were estimated as 99.8% and 0.2% respectively. However in the region influenced by the cosmetic pass, the austenite volume fraction was estimated as 13.7% indicating that an additional thermal cycle has altered the volume fraction significantly.

From Fig. 6, it can be seen that the average grain size in ferrite phase is approximately 4.40 μm whereas the austenite phase grain size is 1.41 μm. Observing Fig. 7, it can be noted that the average grain size in ferrite is approximately 5.25 μm and that in austenite is 4.73 μm. This indicates that further to altering the volume fractions of the respective phases, the additional cosmetic pass has also resulted in slightly increased grain size in the weld fusion zone in both the phases. From the average grain size plot for ferrite phase shown in Figs. 6 and 7 (a) from the weld fusion zone with and without cosmetic pass, it can be seen that the grain size has increased with the application of an additional pass.

The phase map and the orientation map for the HAZ on P91 side are shown in Fig. 8(a) and 8(b) respectively. Similar images for the P91 base material is shown in Fig. 9(a) and (b). Comparing Figs. 8 (a) and 9 (a), it can be clearly distinguished that the HAZ has a definite fine-grained microstructure compared to the parent material which is typically observed in P91 HAZ. The average grain size in the P91 HAZ and parent regions is approximately 4.4 μm and 7.6 μm respectively. It is quite clear that P91 HAZ region has finer grain size.In the EBSD maps presented in this study, it has not been possible to successfully differentiate between bcc (body centred cubic) structured ferrite and bct (body centred tetragonal) structured martensite. The formation of martensite requires

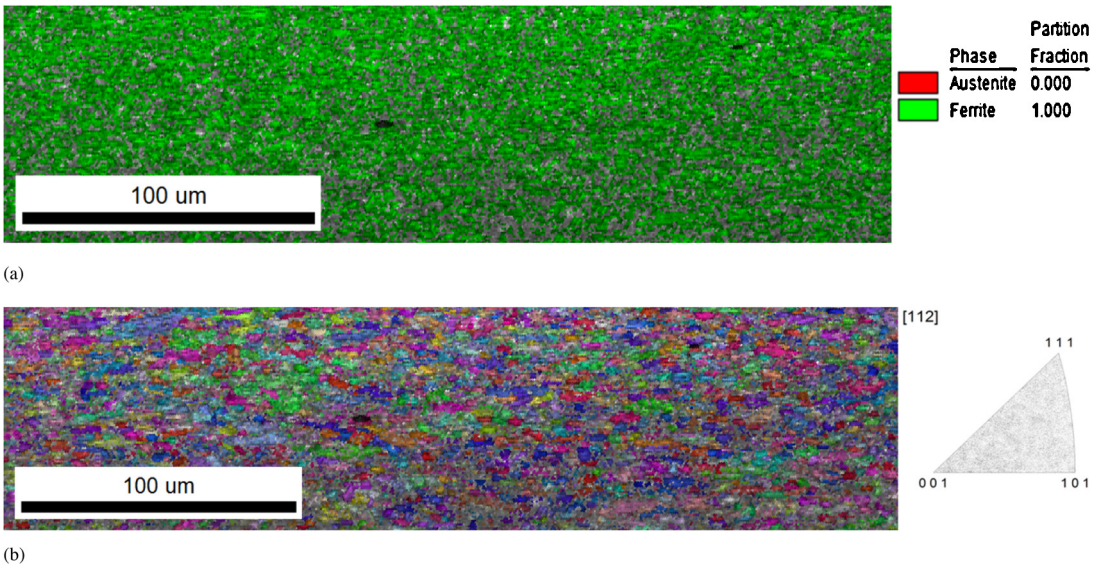

Fig. 8. (a) Phase map and (b) Orientation map for P91 HAZ region.

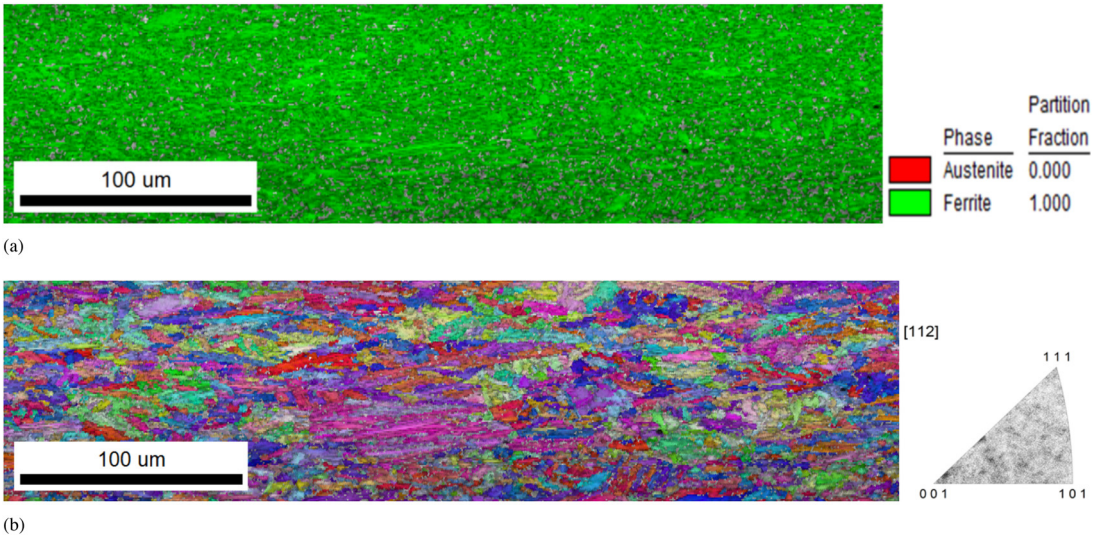

Fig. 9. (a) Phase map and (b) Orientation map for P91 parent region.

rapid cooling of austenite to trap carbon atoms inside a bcc lattice, giving a metastable bct structure. However, the c/a ratio of the lattice is dependent on carbon content and typically is close to one, and as such the structure is very close to being cubic according to Ryde (2006). Conventional EBSD is not capable of distinguishing the difference in the resulting patterns [www.ebsd-image.org]. In essence, where EBSD phase maps show "ferrite" grains these could be martensite.

Given the inability to differentiate between ferrite and martensite using EBSD [www.ebsd-image.org], a Schaeffler-Delong type equation was utilised to estimate the composition of the weld metal. A 1:1 mix of metals have been utilised to give a rough approximation. Ni and Cr equivalents have been calculated using the equations suggested by Fieldstein and Lake (1993) given in Eqs. (1) and (2).

$$Ni_{eq} = \%Ni + 35\%C + 20\%N + 0.25\%Cu \quad (1)$$

$$Cr_{eq} = \%Cr + \%Mo + 0.7\%Nb \quad (2)$$

The resulting region is outside the area presented in the WRC-92 diagram suggested by Kotecki and Siewert (1992) in their research to predict the FN for dissimilar weld. Essentially the authors have utilised the Schaeffler's original diagram proposed by Schaeffler (1949) to identify the phase structure especially in a weld metal as shown in Fig. 10. This puts the material as 'Austenite + Martensite', albeit very close to the 'Austenite + Ferrite + Martensite' boundary. Given the relative positive of the material, it is highly likely the majority of the BCC 'ferrite' detected by EBSD is actually martensite.

In order to further assist in characterising the microstructure of the fusion zone and HAZ in the welded specimen, the hardness of the specimen was measured across the weld at mid-thickness and is shown in Fig. 11. From the hardness map it can be noted that the centre of the weld has considerably high hardness, compared to the surrounding material, indicating that the weld material is martensitic structure rather than ferritic. This correlates well with the previous experience from welding P91 material where martensitic phase formed in the weld during rapid weld cooling cycle due to solid state phase transformation (SSPT) associated with P91 steel as demonstrated by Dai et al. (2008) based on their

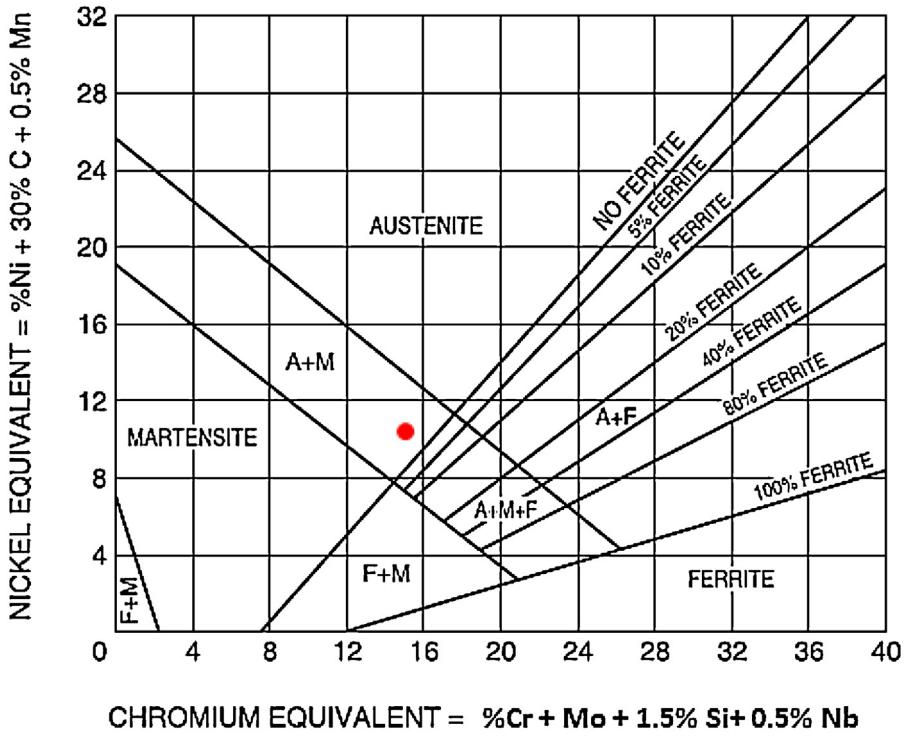

Fig. 10. Schaeffler's original weld composition diagram Schaeffler (1949), the dot shows the expected approximate composition of the weld metal.

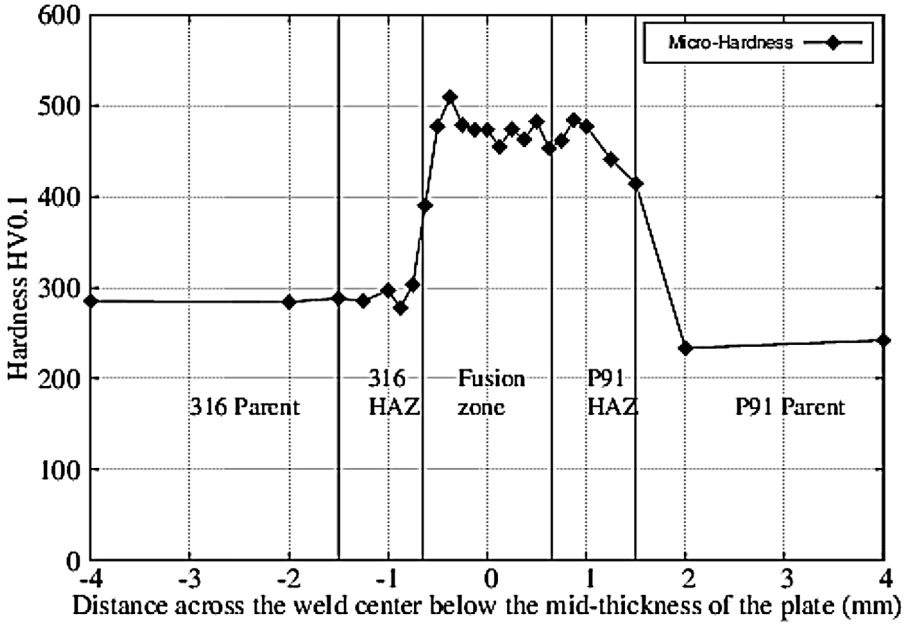

Fig. 11. Micro-hardness across the weld at mid-thickness for the dissimilar weld pad.

work in characterising phase transformations in ferritic steels using x-ray and neutron diffraction as well as by Dean and Hidekazu (2006) through FE simulation of welding of P91 steel considering the mechanical effects of SSPT in their analysis. Yaghi et al. (2007) predicted compressive stresses in the weld centre through simulation of multipass TIG welding of P91 pipes which they explained through SSPT during rapid cooling of the weld pool. Finally Kim et al. (2009) concluded the same in their analysis of residual stresses in P91 steel weld through FE and corroborated their predictions through detailed neutron diffraction analysis of the welded plates.

In agreement to the previous research on P91 weld material, it was concluded in the current study that the weld material is indeed martensite. Based on the measured hardness values (> 450 Hv0.1) it is clearly seen that the extent of the martensitic zone extends from fusion zone to HAZ on P91 side roughly measuring 2 mm wide.Application of microstructure information to neutron diffraction data analysis

Based on the phase volume fraction obtained from the EBSD experiment, the data analysis of residual stress on the welded plate from neutron diffraction was extended to calculate the overall

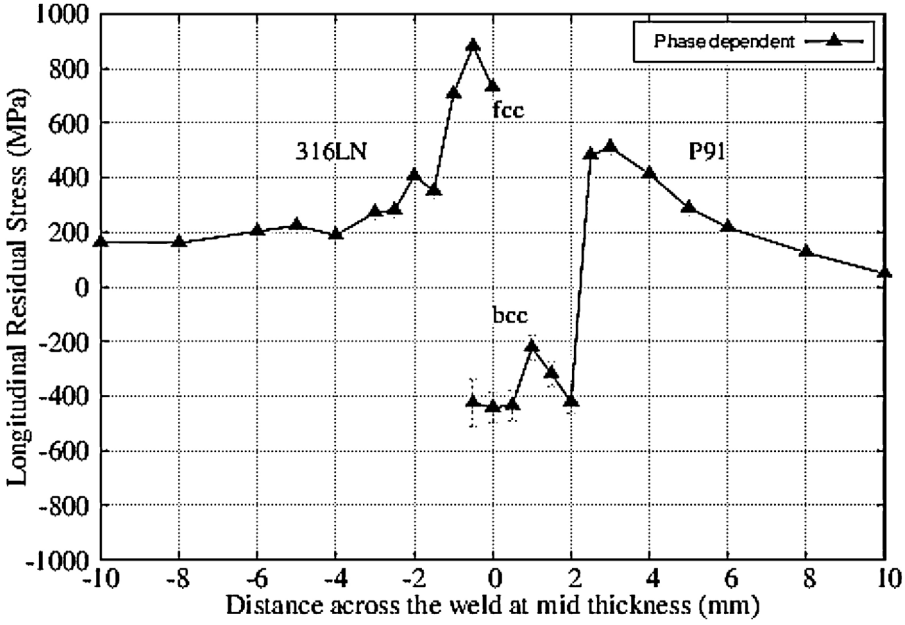

Fig. 12. Phase characteristic macrostress for the fcc and bcc phase is the weld fusion and HAZ regions (Abburi Venkata et al. 2015).

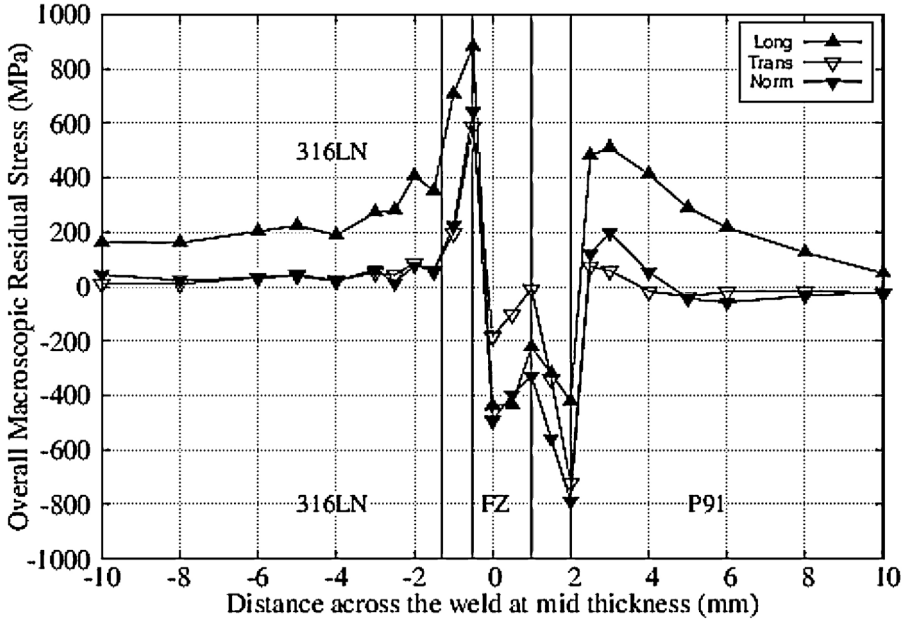

Fig. 13. Overall macro residual stress profile across the weld at mid-thickness.

residual stress state in a dissimilar EB welded plate made from P91 and 316LN materials. The experiment was conducted on the time-of-flight instrument ENGIN-X at ISIS, RAL facility in UK. Pawley (1981) suggested a refinement for obtaining the best possible unit cell from diffraction data. The diffraction peaks from neutron diffraction were fit using Pawley-Rietveld refinement. Owing to the narrow width of the weld fusion zone and HAZ, a gauge volume of 1 mm x 1 mm x 1 mm was employed for neutron diffraction measurement across the weld, to capture the steep gradients of residual stress over small length scale. The details of the sample, d_0 specimens and neutron diffraction experiment were explained fully by Abburi Venkata et al. (2015) and Abburi Venkata et al. (2016) in their research on characterising residual stresses in a dissimilar EB welded plate and residual stress relaxation through specimen extraction in a dissimilar EB weld respectively.

The measured residual stress profile across the weld at mid-thickness of the specimen is shown in Fig. 12 as published in Abburi Venkata et al. (2015). After careful and thorough analysis it was agreed that the measured residual stresses corresponded to the macroscopic stress characteristic of each phase, rather than the continuum average as discussed in Abburi Venkata et al. (2015) and Abburi Venkata et al. (2016). It can be seen that the disconnected profile resulting from the tensile (fcc phase) to compressive (bcc phase) shift is indicative of the phase characteristic macrostress rather than the overall macrostress state. The overall macro-scale stress can be approximated using the summation of the stresses characteristic of each phase measured from neutron diffraction as suggested by Hutchings et al. (2005) in their book on neutron diffraction for residual stress measurement. The overall macro-

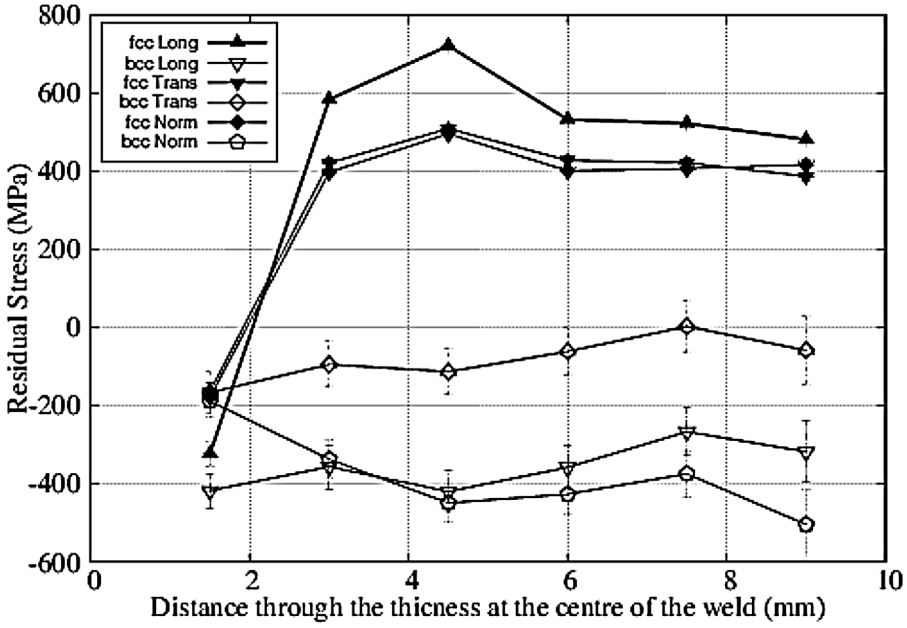

Fig. 14. Phase characteristic macrostress through the thickness at the weld centre Abburi Venkata et al. (2015).

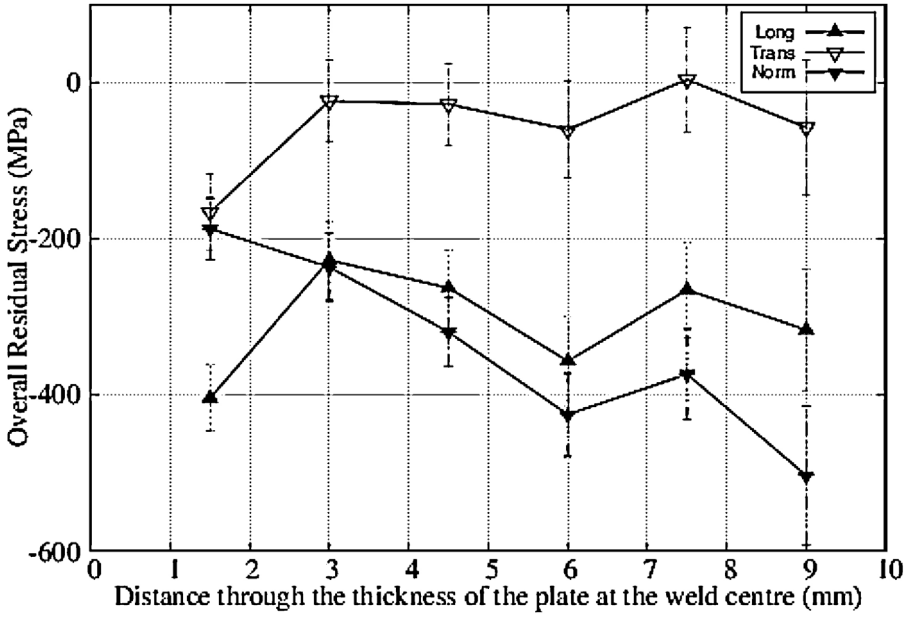

Fig. 15. Overall macrostress through the thickness at the weld centre.

scale residual stress can be given by Eq.(3) described by Lodini (2003).

$$\sigma_{ij}^{I} = f\left(\sigma_{ij}^{ph1}\right) + (1-f)\sigma_{ij}^{ph2} \tag{3}$$

where ${\sigma^I}_{ij}$ is the overall macrostress, ${\sigma^{ph1}}_{ij}$ is the macrostress characteristic of phase 1, f is the phase volume of phase 1, ${\sigma^{ph2}}_{ij}$ is the macrostress characteristic of phase 2. From the EBSD experiment the phase fractions have been determined for the fusion zone and HAZ regions. Based on these phase fractions, the overall macroscale residual stress is calculated across the weld at mid-thickness of the sample. The overall macroscale residual stress profile across the weld at mid-thickness is shown in Fig. 13.

Comparing the overall macrostress shown in Fig. 13 with the phase characteristic macrostress profile measured across the weld at mid-thickness as illustrated in Fig. 12, it can be seen that the disconnected stress profile is now represented as a smooth continuous line. It is interesting to note that the overall macrostress profile correlates closely with the hardness profile shown in Fig. 11. The weld fusion zone is under compression presumably from the SSPT associated with martensitic formation and the extent of this compressive zone corresponds well with that of the high hardness depicted in the hardness map which is characteristic of martensitic phase. Also the tensile peaks are pushed into softer zones adjacent to the weld fusion zone on 316LN side and next to the HAZ on the P91 side.

Similarly the through-thickness distributions of phase characteristic macrostress measured at the centre of the weld using neutron diffraction for bcc and fcc phases are shown in Fig. 14. From the graph it can be noticed quite clearly that the fcc phase in the weld fusion zone is predominantly under tension, whereas

the bcc phase is under tension. It is evident from this that the measured stresses were phase characteristic macrostresses rather than the overall residual macrostress profile. However substituting the relative volume fractions of the bcc and fcc phases as suited for the regions under the influence of cosmetic pass and away from it, an overall macrostress profile was obtained as shown in Fig. 15. Looking at the stress profile in Fig. 15, it can be established that the weld centre is predominantly under general compression which is explained from the volumetric changes associated with SSPT of ferrite to martensite during rapid cooling of the weld pool.Conclusions

Based on the microstructural analysis of the dissimilar weld joint using EBSD, the following conclusions can be drawn:

1. The weld fusion zone of a dissimilar metal weld between P91 ferritic/martensitic steel and AISI 316LN austenitic stainless steel is predominantly ferritic with traces of austenite. However the percentage of austenite has increased with the application of another thermal cycle as a cosmetic pass in this instance.
2. Incorporating the volume phase fraction of each phase, associated with the weld and HAZ regions, in the neutron diffraction data analysis has resulted in an overall residual stress state that is compressive in the weld centre and the HAZ of the P91 side. Tensile stress in the fcc phase is insignificant due to the small phase fraction of austenite compared to ferrite.
3. The prevailing compressive residual stress state is the direct result of the volume change associated with the solid state phase transformation of ferrite to martensite during rapid cooling of the weld pool and the considerable mismatch in the base material properties for P91 and 316LN materials.
4. The extent of the overall compressive macroscopic residual stress profile in the fusion zone and HAZ calculated from the phase volume fractions correlates very well with that of the measured micro hardness profile in the fusion zone, thereby asserting the presence and influence of martensite.

Acknowledgements

We would like to acknowledge the support provided by IGCAR for the samples and ISIS at Oxford, for the valuable advice and support to the residual stress measurements. This project was funded by an EPSRC project EP/K007866/1.

References

Abburi Venkata, K., Truman, C.E., Smith, D.J., 2015. Characterising residual stresses in a dissimilar metal electron beam welded plate. Procedia Eng. 130, 973–985.
Abburi Venkata, K., Truman, C.E., Smith, D.J., Bhaduri, A.K., 2016. Characterising electron beam welded dissimilar metal joints to study residual stress relaxation from specimen extraction. Int. J. Press. Vessels Pip. 139–140, 237–249.
Abson, D.J., Rothwell, J.S., 2013. Review of type IV cracking of weldments in 9–12% Cr creep strength enhanced ferritic steels. Inter. Mater. Rev. 58 (8), 437–473.
Bala Srinivasan, P., Muthupandi, V., Sivan, V., Bala Srinivasan, P., Dietzel, W., 2006. Microstructure and corrosion behaviour of shielded metal arc-welded dissimilar joints comprising duplex stainless steel and low alloy steel. J. Mater. Eng. Perform. 15 (6), 758–764.
Barnhouse, E.J., Lippold, J.C., 1998. Microstructure/property relationships in a dissimilar welds between duplex stainless steels and carbon steels. Weld. J. 77 (12), 477s–487s.
Benjamin, F., Maxime, S., Alexandra, R., Francoise, B., Andre, P., 2009. Microstructural evolutions and cyclic softening of 9% Cr martensitic steels. J. Nucl. Mater. 386–388, 71–74.
Chatterjee, S., Abinandanan, T.A., Reddy, G.M., Chattopadhyay, K., 2016. Microstructure formation in dissimilar metal welds: electron beam welding of Ti/Ni. Metall. Mater. Trans. A 47A, 769–776.
Dai, H., Francis, J.A., Stone, H.J., Bhadesia, H.K.D.H., Withers, P.J., 2008. Characterizing phase transformations and their effects on ferritic weld residual stresses with x-rays and neutrons. Metall. Mater. Trans. A 39A, 3070–3078.
Dawson, K.E., 2012. Dissimilar Metal Welds. University of Liverpool (PhD thesis).
Dean, D., Hidekazu, M., 2006. Prediction of welding residual stress in multi-pass butt-welded modified 9Cr-1Mo steel pipe considering phase transformation effects. Comput. Mater. Sci. 37, 209–219.
Ferro, P., Berto, F., 2016. Quantification of the influence of residual stresses on fatigue strength of Al-alloy welded joints by means of local strain energy density approach. Strength Mater. 48 (3), 426–436.
Fieldstein, J., Lake, F., 1993. A new constitution diagram for predicting ferrite content of stainless steel weld metals. Mater. Des. 14 (6), 345–348, http://dx.doi.org/10.1016/0261-3069(93)90110-H.
Hajri, M.A., Malik, A.U., Meroufel, A., Al-Muaili, F., 2015. Permature failure of dissimilar metal weld joint at intermediate temperature superheater tube: case study. Case Stud. Eng. Fail. Anal. 3, 96–103.
Hutchings, M.T., Withers, P.J., Holden, T.M., Lorentzen, T., 2005. Introduction to the Characterization of Residual Stress by Neutron Diffraction. CRC Press, Taylor & Francis Group.
Kerr, M., Prime, M.B., Swenson, H., Beuchler, M.A., Steinzig, M., Clausen, B., Sisneros, T., 2013. Residual stress characterization in a dissimilar metal weld nuclear reactor piping system mock-up. J. Press. Vessel Technol. 135 (4), 041205–041218.
Kim, S.-H., Kim, J.-B., Lee, W.J., 2009. Numerical prediction and neutron diffraction measurement of the residual stresses for a modified 9Cr-1Mo steel weld. J. Mater. Process. Technol. 209, 3905–3913.
Kotecki, D.J., Siewert, T.A., 1992. WRC-1992 constitution diagram for stainless steel weld metals: a modification of the WRC-1988 diagram. Weld. Res. Supp., 171–178.
Lazzarin, P., Tovo, R., 1998. A notch intensity factor approach to the stress analysis of welds. Fatigue Fract. Eng. Mater. Struct. 21, 1089–1103.
Lodini, A., 2003. Calculation of residual stress from measured strain. In: Lodini, A., Fitzpatrick, M.E. (Eds.), Analysis of Residual Stress by Diffraction Using Neutron and Synchrotron Radiation. Taylor & Francis, London and New York, pp. 47–59.
Mvola, B., Kah, P., Martikainen, J., 2014. Dissimilar ferrous metal welding using advanced gas metal arc welding processes. Rev. Adv. Mater. Sci. 38, 125–137.
Ohms, C., Martins, R.V., 2014. Investigation of residual stress/strain and texture in a large dissimilar metal weld using synchrotron radiation and neutrons. Mater. Sci. Forum 772, 193–199.
Pawley, G.S., 1981. Unit cell refinement from powder diffraction scans. J. Appl. Crystallogr. 14, 357–361.
Randle, V., 2009. Applications of electron backscatter diffraction to materials science: status in 2009. J. Mater. Sci. 44, 4211–4218.
Ruiz-Hervias, J., Iordachescu, M., Luzin, V., Law, M., Iordachescu, D., Ocaña, J.L., 2014. Residual stress distributions in bi-metal (ferritic to austenitic steel) joints made by laser welding. Mater. Sci. Forum 772, 181–185.
Ryde, L., 2006. Application of EBSD to analysis of microstructure in commercial steels. Mater. Sci. Tech. 22 (11), 1297–1306.
Schaeffler, A.L., 1949. Constitution diagram for stainless steel weld metal. Met. Prog. 56 (11), 680.
Shahid, F., Khan, A.A., Saqib Hameed, M., 2015. Mechanical and microstructural analysis of dissimilar metal welds. Int. J. Recent Res. Appl. Stud. 25 (1), 6–14.
Dye, D., Stone, H.J., Reed, R.C., 2001. Intergranular and interphase microstresses. Curr. Opin. Solid State Mater. Sci. 5, 31–37.
Sun, Z., Karppi, R., 1996. The application of electron beam welding for the joining of dissimilar metals: an overview. J. Mater. Process. Technol. 59, 257–267.
Ueji, R., Fujii, H., Ninomiya, T., Mino, A., 2013. Microstructure evolution in dissimilar metal joint interface obtained by friction stir welding of cast iron and carbon steel. Trans. JWRI 42 (1), 33–37.
Winkelmann, A., Nolze, G., Vos, M., Salvat-Pujol, F., Werner, W.S.M., 2016. Physics-based simulation models for EBSD: advances and challenges. Mater. Sci. Eng. 109, http://dx.doi.org/10.1088/1757-899X/109/1/012018.
Yaghi, A.H., Hyde, T.H., Becker, A.A., Sun, W., 2007. Numerical simulation of P91 pipe welding including the effects of solid-state phase transformation on residual stresses. JMDA 221, 213–224.